Sixth International Symposium on Marine Propulsors
smp'19, Rome, Italy, May 2019

Hydroacoustical Calculations On A Generic Underwater Vehicle Using Lighthill-Curle Formulations

Emre Güngör[1]

[1]Roketsan Technology Research Center (ROTAM), Istanbul, Turkey

ABSTRACT

In this paper, the hydroacoustical calculations are performed on a generic underwater vehicle and its propulsion system using numerical solvers. Sound pressure level, sound directivity, acoustical spectrum and acoustical patterns are investigated with the aid of finite volume method and hybrid acoustical analogies such as Lighthill-Curle method. In order to validate those calculation tecniques, the results are compared with testcases in which pressure data is obtained using pressure transducers and microphones. So as to determine proper solver type, discretization schema, mesh size and acoustical analogy, the validations are performed in two step, namely hydrodynamical calculations and acoustical solutions. A single propeller 4382 is subjected to an homogenous flow at different rotation rates and inflow velocities. Large Eddy Simulation (LES) is implemented to solve turbulence quantities and filter large eddies in equations. Thrust and torque results are matching well in the region of on and off-design conditions with a low error range. A test case in which the pressure pulses resulted from single propeller VP1304 is also investigated. In this case, monopole, dipole and quadrupole source terms are attained from CFD calculations to couple them with acoustical solutions. The first three harmonics of the fluctuations are investigated and compared with respect to those of the experimental data. Except for the second sensor, the matching is well nice at each harmonic. Using the verified method, the generic underwater vehicle body is supposed to be propelled by the CRP with a specific design rpm. The contributions of different sound sources on the generic underwater vehicle body which is supposed to be propelled by the Counter-rotating Propeller (CRP) is observed and classified with respect to their frequency levels. Regarding to the spectrum of the CRP system, the blade passing frequency, the harmonics and tonal noises are also clearly identified.

Keywords

Lighthill, hydroacoustic, sound spectrum, counter-rotating propeller, underwater vehicle,

1 INTRODUCTION

Computational methods have gained momentum due to the development of high-speed computer technology in recent years. In the present day, it is possible to solve many flow-originated engineering problems with commercial software. The most realistic solution is Direct Numerical Simulation (DNS) by which the turbulence scales are solved without the need for a model. However, especially in the case of high Reynolds numbers, the computer capacity seems to be unfeasible except for low Reynolds numbers and simple geometries. Another commonly used method to simulate problems related with Computational Fluid Dynamics is the Reynolds Average Navier-Stokes (RANS). However, the use of acoustic field is also limited because only average flow is addressed and high dependency on turbulence models is concerned. Instead, Large Eddy Simulation (LES) in preferred in where large-scale structures are directly solved and small-scale ones are modeled. Experimental data must be studied to compare the success of all these methods. As an example, the experimental evaluation of the CFD methods in the hydrodynamic field is described by Brizzolara et al. (2011) on the propeller. Test data for the propeller VP1304 in the Potsdam tunnel were shared with the participants and a comparison of their methods was provided [1]. For a similar underwater problem, evaluation of mesh, turbulence model and analysis results in CFD software was done by Güngör and Özdemir [2]. For non-homogeneous multiphase flows, CFD solutions are presented in previous study by Güngör [3] and pressure fluctuations are calculated to obtain the information of noise spectrum. On the other hand, Sovani and Chen [4] performed aerodynamic calculations of raingutter in the CFD environment before the aeroacoustic solutions. Then the noise was estimated by feeding the results to the Ffowcs Williams Hawkings (FWH) formulation. Rumpfkeil [5] also compared aerodynamic sound propagation by using different techniques and test data. Unlike these, the integral modeling of hydrodynamics and hydroacoustics based on the Boundary Element Method (BEM) technique instead of the Finite Element Method (FEM) is described by Salvatore et al. [6]. In terms of computer capacity requirements, the Lighthill approach, Curle formulation, FWH approach, Kirschhoff method and their extensions, which are based on the use of Green function instead of volume discretized methods, are generally preferred.

However, when referring to complex geometries and structural interactions it is necessary to refer to volume discretized methods (finite differences, discontinuous Galerkin, finite volume, finite element method). In these methods, linearized Euler and Lighthill equations are solved. Oberai et al. [7] have converted Lighthill's wave propagation equations in a weak, variational form to be applicable to the finite element method using a weighted residual method. Here the weak form wave equation is multiplied by a test function and is integrated throughout the whole volume. Thus, terms such as unknown pressure can be found in matrix solutions.

2 FLOW EQUATIONS AND NUMERICAL SOLUTION

The conservation equations on fluid dynamics can be applied to an infinitesimal fixed volume flow element. Thus, the conservation of mass,

$$\frac{\partial \rho}{\partial t} + \frac{\partial \rho u_i}{\partial x_i} = 0 \tag{1}$$

and conservation of momentum,

$$\frac{\partial \rho u_i}{\partial t} + \frac{\partial \rho u_i u_j}{\partial x_j} = -\frac{\partial (p\delta_{ij} - \sigma_{ij})}{\partial x_j} + f_i \tag{2}$$

in which pressure, viscous strain tensor and external force are given respectively. In the presence of a suitable model for the viscous strain tensor, these equations are transformed into Navier-Stokes equations. Momentum and mass transport are largely through large eddies that these are very much affected by geometry and boundary conditions unlike small ones. Filtering is required to find the flow velocity field containing large-scale structures.

$$\bar{u}_i(x) = \int K(x, x') u_i(x') dx' \tag{3}$$

The Kernel function which includes the local average and the cutting length is used to determine flow velocity field. While larger vortices are resolved from the filtered scale, the smaller ones are modeled. When the incompressible flow is subjected to filtration, the momentum and mass equations can be attained as,

$$\frac{\partial \rho \bar{u}_i}{\partial t} + \frac{\partial \left(\rho \overline{u_i u_j}\right)}{\partial x_i} = -\frac{\partial \bar{p}}{\partial x_j} + \frac{\partial}{\partial x_j}\left[\mu\left(\frac{\partial \bar{u}_i}{\partial x_j} + \frac{\partial \bar{u}_j}{\partial x_i}\right)\right] \tag{4}$$

$$\frac{\partial \rho \bar{u}_i}{\partial x_i} = 0 \tag{5}$$

Subgrid-scale Reynolds Stress (SRS) describes the momentum flux resulting from the interaction of small-scale structures that need to be modeled.

$$\tau_{ij}^s = -\rho\left[\left(\overline{\rho u_i u_j}\right) - \bar{u}_i \bar{u}_j\right] \tag{6}$$

Smagorinsky [8] suggested an equation in that the right side contains the strain rate of large scales and vortex viscosity. Using the pressure-based solver, the velocity field can be found in the pressure correction equation.

$$\tau_{ij}^s - \frac{1}{3}\tau_{ij}^s \delta_{ij} = \mu_t\left(\frac{\partial \bar{u}_i}{\partial x_j} + \frac{\partial \bar{u}_j}{\partial x_i}\right) \tag{7}$$

The rotation of the propeller can be modeled via sliding mesh mechanism. The relative velocity with respect to rotating frame can be attained as,

$$u_r = u - \Omega_p x r \tag{8}$$

Substitution of relative velocity in the continuity equation gives,

$$\frac{\partial \rho}{\partial t} + \frac{\partial \rho u_r}{\partial x_i} = S_m \tag{9}$$

When writing the momentum equation in terms of relative velocity, the right side of the equation is given as,

$$\frac{\partial \rho u}{\partial t} + \nabla \cdot (\rho u_r u_r) + 2\Omega \times u_r + \Omega \times \Omega \times r + \rho \frac{\partial \Omega}{\partial t} \times r \tag{10}$$

3 ACOUSTICAL EQUATIONS

When it is taken the time derivative of the mass conservation equation and substract from the divergence of the momentum equation,

$$\frac{\partial^2 \rho}{\partial t^2} = \frac{\partial^2}{\partial x_i \partial x_j}\left(\frac{\partial (p\delta_{ij} - \sigma_{ij} + \rho u_i u_j)}{\partial x_j}\right) - \frac{\partial f_i}{\partial x_i} \tag{11}$$

Lighthill analogy can be attained after removing the term from both sides of this equation,

$$\frac{1}{{c_o}^2}\frac{\partial^2 p'}{\partial t^2} - \frac{\partial^2 p'}{\partial {x_i}^2} = \frac{\partial^2}{\partial x_i \partial x_j}\left(\rho u_i u_j - \sigma_{ij}\right) - \frac{\partial f_i}{\partial x_i} + \frac{\partial^2}{\partial t^2}\left(\frac{p'}{{c_o}^2} - \rho'\right) \tag{12}$$

Curle [9] extended the Lighthill analogy for flows in presence of walls. In order to solve the wave equation, he applied Green functions of surface integrals on S and volume integrals in volume V.

The first integral on the right is the term quadrupole and is defined in the flow volume region while the second term is called monopole representing the mass flux deviation in time. The last integral is taken along the surface and is defined as the response of the wall to the flow force, namely dipole sound source. The time-dependent variation of the flow rate within the volume reveals the quadrupole source. On the other hand, dipole sources are generated by the development of turbulent boundary layers on stationary surfaces and require knowledge of pressure data over time.

---

[*] Leave blank the last 2.0 cm on the first page to place some additional informational about this paper in a footnote on the first page if necessary.

3 ACOUSTICAL METHOD VALIDATIONS

3.1 Validation on Propeller 4382

The sound source required to solve the acoustic equations is obtained from the pressure data obtained in the flow dynamics solutions. Besides, numerical simulation and modeling of flow dynamics should be verified in the first stage. For this purpose, the data of 4382 propeller tested by Boswell [10] were compared with numerical results. Dimensionless parameters that represent the performance of the propeller are the advance, thrust, and torque coefficients.

$$K_t = \frac{T}{\rho \Omega_P{}^2 D^4} \qquad K_q = \frac{Q}{\rho \Omega_P{}^2 D^5} \qquad J = \frac{u}{\Omega_P D} \tag{13}$$

The diameter of the testcase propeller is 0.305 m and rotating at about 468 rpm. The unstructured mesh of approximately 8 million in the flow volume is formed in a similar manner to that of Figure 1.

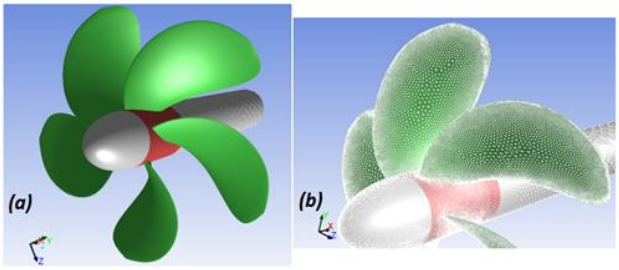

Figure 1. (a) CAD model of propeller 4382 and (b) fine mesh generated

The flow volume is formed ten times wider than the diameter of the propeller. The inlet is defined as constant flow velocity while the far field is defined as constant pressure. Boundary layer is formed on the surfaces representing y+<3.0. Time-dependent results are obtained with LES in the pressure-based solver. Second order discretizations are preferred to increase accuracy. Although the calculations are compatible with the experimental data, a small deviation from the test results is observed in the low and high advanced coefficients. This is due to the excess of separation on the blades at high revolution rate or high flow velocity, and the excessive irregularity of the wake behind the propeller.

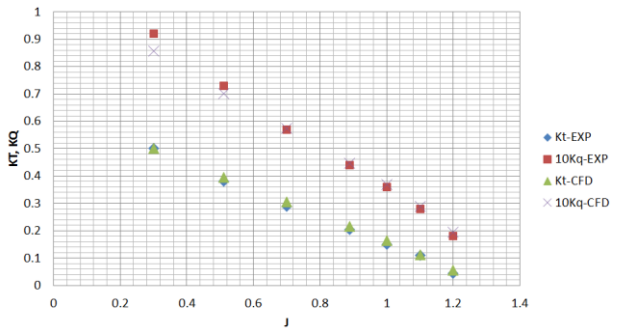

Figure 2. Comparison of numerical and experimental results for Propeller 4382

3.2 Validation on Propeller 4382

In order to tune the CFD tools for the analysis of new designs, the solver settings and preferences in software should be validated against experimental results attained in facilities which are arranged for almost similar applications. In this manner, the tests of the rotating propeller on an inclined shaft were carried out by Potsdam [11] in cavitation tunnel. The pressure oscillations are measured by placing the receivers as shown in Figure 3 and test-specific parameters are given in Table 1. The rotation of the impeller can be modeled by applying flow conditions and a moving reference frame method. The flow rate in the tunnel is determined for each operation point and it is given as a boundary condition by considering the advance coefficient and propeller revolution. The outermost surface of the flow volume can be defined as constant pressure. Due to the minimum effects of tunnel wall boundaries, those are not modeled in process. An unstructured tetrahedral mesh type with approximately seven million cells is preferred and LES solution is applied to attain time dependent results. In the vicinity of the blade, on the trailing and leading edges, a very tight mesh is formed and the accuracy is increased. The time step is selected to be 1°, but smaller time steps are not preferred because of the increase in solution time. Hence, the solution time for a computer with 16 processors is about 80 hours.

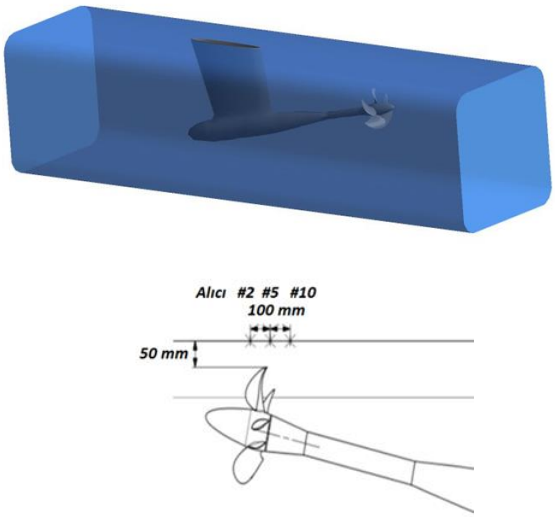

Figure 3. Representation of VP1304 propeller in cavitation tunnel and the position of transducers

Pressure data in CFD solutions are used as source information and the validity of the Lighthill-Curle analogy is obtained by placing certain points on the receiver. Due to the presence of moving surfaces, monopole sources are common in such cases. The blade passing frequencies have been shown to be the dominant source while the quadrupole terms affect broad and high-band ranges. Dipole terms provide a significant contribution to noise as the pressure on the surface is

changed over time. Three harmonic amplitudes have been tried to be found at the blade passing frequencies.

Table 1: Parameters for test setup

Properties	Symbol	Unit	Value
Advanced Coefficient	J	-	1.019
Propeller rotation rate	Ω_P	1/s	20
Density	ρ	kg/m^3	997.38
Viscosity	ν	m^2/s	9.199E-07
Inclination angle	φ	°	12

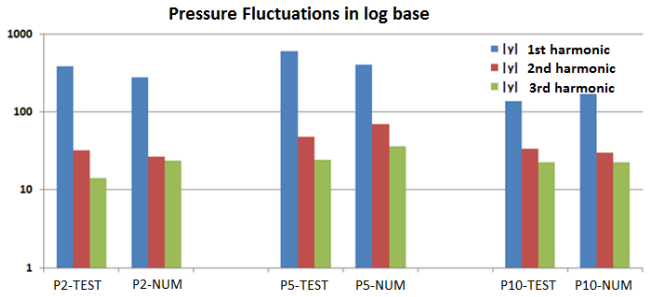

Figure 4. CFD and Experiment Comparison of VP1304 at different harmonics

Non-reflecting boundary condition is assigned to the test tunnel walls so that there is no sound reflection. The far field density, sound velocity and reference acoustic pressure values are selected as 1020 kg/m3, 1050 m/s and 10-5 Pa. The analysis results and the test data are compared in Figure 4 considering the harmonics. As the first (# 2) and second (# 5) pressure sensors are close to the blade tip points, the amplitudes are the highest. The numerical results other than the first harmonic of the second sensor are consistent with the test data. The second and third harmonics in all sensors are scaled to log-base make it easy to compare. Blade passing frequencies in the spectrum can be easily observed. As a result of the non-homogeneous flow, the first harmonics deviate a certain amount since the instantaneous oscillations at the blade tips are in high order. Beyond the second harmonics, the diagnosis of the amplitudes is very difficult. On the other hand, it is estimated that the variation in amplitudes may also be due to the test data. Although the outside noise is eliminated during the test, the results may include additional amplitudes from the vibrating noise that will occur with the operation of the propeller in the water. The presence of these effects has been neglected in the test.

4 HYDROACOUSTICAL CALCULATIONS FOR A GENERIC UNDERWATER VEHICLE

Finite volume calculations are carried out via commercial software on the generic underwater vehicle body form and propulsion system of CRP. Thus, the sound source information is stored for hydroacoustic studies by solving the flow dynamics. Time-dependent LES analyzes are performed using the validated methods and parameters, and a certain period of angular rotation of the two propellers is modeled by the sliding mesh method. In every step, the solution of the previous time step by using the pressure, velocity and turbulent structure properties is going to be solved. The solid model of the body and propeller system is shown in Figure 5.

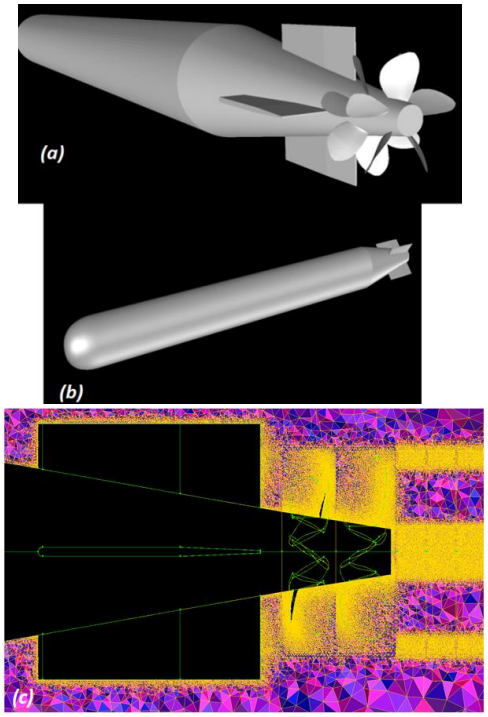

Figure 5. Representation of generic underwater vehicle with and without propeller

The generic underwater vehicle has a length of 5.20 m and a diameter of 0.67 m. The 7-bladed propeller near the body is called the front propeller, and the other 5-bladed propeller is called the rear propeller. The diameters are 0.62 m and 0.58 m respectively. A total of 4 rudders are found, but the zero angle position is maintained within the scope of the analysis. As the vehicle travels at a speed of 30 kts, the front propeller rotates at 650 rpm and the rear one rotates at 500 rpm. In order to validate mesh dependency factor, In addition, the mesh structure on the propeller side is densified as much as possible to obtain the finer mesh structure behind the propeller as shown in Fig. 5 and to capture the wake and vortices that is shedding from the blade tips and hub-core region. Axial force in simulation is calculated on body by different mesh types and representation of coarse & medium mesh is given in Figure 6. When the mesh size is compared medium mesh is found to be sufficient to simulate axial force. Therefore a flow volume of ten times the size of the vehicle is selected and a total of 25 million mesh structure (medium) is created.

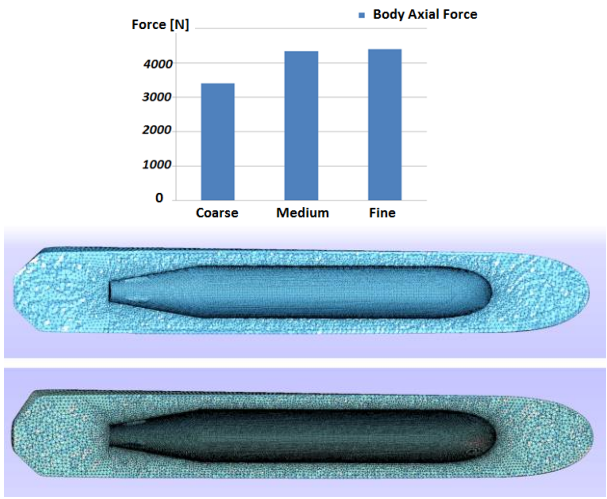

Figure 6. Axial force in simulation calculated on body by different mesh types and representation of coarse & medium mesh

A total of 10 boundary layers are laid out and the first layer thickness y+ value is determined to be below 3.5. In addition, the y+ value is lowered to 1.0 due to the viscous effects on the body being strong. The analysis is attempted to converge until the torque and thrust value of the propeller are obtained. After that, the analysis continued until 5 full rotations and pressure record is created for hydroacoustic analysis. The time step-size is selected around 0.000277 sec in order to achieve frequency range up to 1800 Hz maximum where the resolution of bandwidth is around 1 Hz. Sound pressure level from pressure transducers located at different locations, sound directivity around vehicle, acoustical pattern is investigated by hydroacoustical calculations. Moreover, contributions of the rudder, the cap, the hub, the blade tip on the noise are examined using power spectral density.

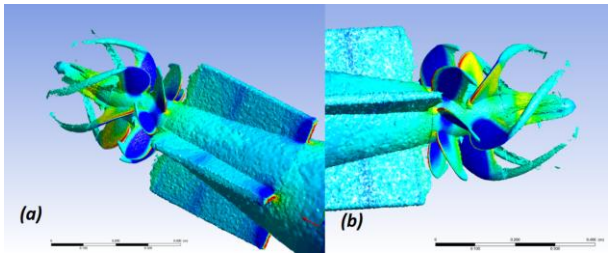

Figure 7. Representation of pressure contours on rudders and akustical wake behind CRP

A coarse and fine mesh pattern is created to observe the effect of the acoustic mesh. Under the fine mesh structure (~ 1.8 million cells), about 90 GB of memory is required when the sources on the body are taken into consideration and the solution is taken in 8 hours using a 16-core processor. By this type of mesh structure, approximately 10 Hz band resolution could be attained. On the other hand, in the coarse mesh structure (~ 0.8 million), the same processors are used to solve the problem in 2.5 hours. A 10 Hz resolution band is not required under computer requirements. As can be seen from the results, it is seen that the rough network structure is sufficient for low and high band. In the middle band, a difference of 20% is observed at some frequencies. For this reason, fine mesh structure is preferred in much cases and coarse mesh is applied in cases where solution with high frequency resolution is requid.

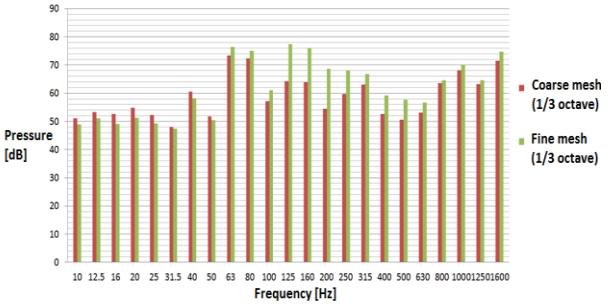

Figure 8. Investigation of the effect of mesh dependency in octave band

Because it contains high amplitude information, the sound directivity characteristic at the frequency of 260 Hz point is shown in polar coordinates as in Figure 9. Induced noise is generated at the front of the propeller in the frequency region of 260 Hz and scattered backwards from the hub, while the amount of scatter and directivity graphs vary for different frequency zones. Acoustic noise can also be seen in the nose region. It should be noted that the amplitude levels only contain flow information and does not contain any vibroacoustic information. Although 10 Hz is not enough for frequency resolution, spectrum chart can be used to investigate acoustical classification. In the axial direction, the acoustic sensor 1 is located at a distance of 1 m from the propeller, the sensor 2 is located at a distance of 1 m from the center of the body in the vertical plane, and the last sensor at a distance of 1 m from the body of the body is defined as the sensor 3.

The logarithmic amplitudes of the noise frequency range where the sound is emitted from body are given in Figure 10. Propeller harmonics are clearly seen around the lower band, but dominant classes are seen as harmonics at frequencies of 140 Hz, 210 Hz and 280 Hz. These classes are thought to originate from the pressure induction of the propeller to the conical surfaces behind the body. The cross sections of the four rudders are 0.040 m on average so they should be apparent at 1540 Hz. Considering the dimension scale representation, the frequency of 800-1100 Hz is the reflection of the vortices that are shed off from the rudder sections. When the sensor 1 data is examined, this frequency line is dominant because it is influenced by the noise sources immediately behind the propeller blades. Another high noise source is the rudders, which show themselves around 1480 Hz. It is also obviously apparent at sensor 2. Despite everything, the most dominant sources are the acoustic traces of the propeller blade passing frequencies, which has been confirmed for all sensors. As the pressure information for much higher frequencies can not be obtained on the

hydrodynamic side, much of the frequency range keep the acoustic power high towards the 1800 Hz band. However, if much higher frequencies would be maintained, the acoustic power and correspondingly the decrease in amplitude levels could be observed clearly.

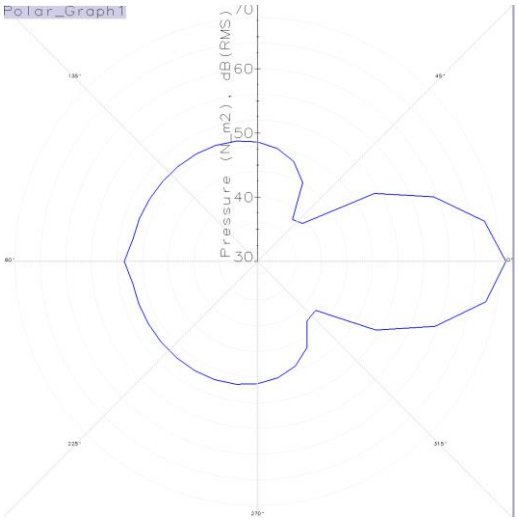

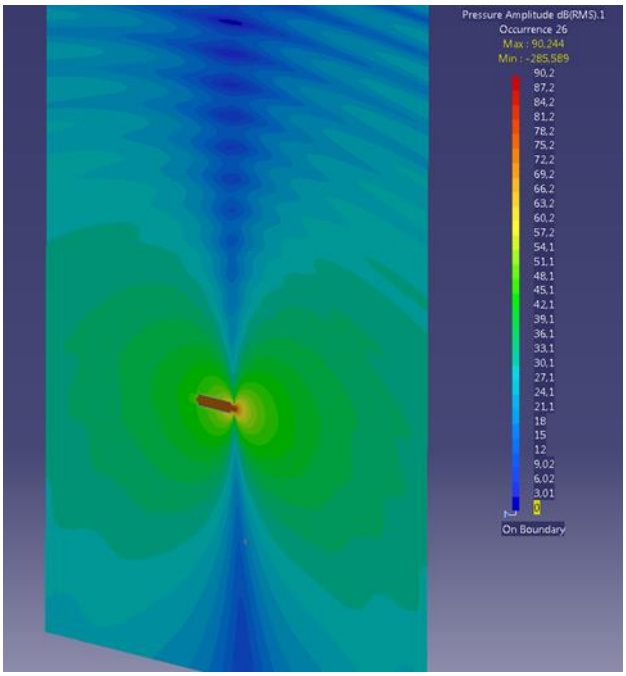

Figure 9. Directivity of radiated noise from body in polar coordinates and pressure amplitude variations on plane at 260 Hz

The pressure data is measured from two sensors which are placed at angles of zero and ninety degrees to the propeller respectively. As shown in Figure 10, frequency of 42 Hz and 74 Hz correspond to the blade passing frequencies of the front and rear propellers while 85 Hz and 145 Hz indicate second harmonics. Third harmonics seem to be damped in high order, while the sources formed by turbulent structures dominate at the frequency of 800 to 1200 Hz. Since the cross-sections of the blades are 0.015 m on average, the acoustic scale level is 15.42/0.015 and it shows itself at 1000 Hz. The amplitude at 270 Hz region might be the result of hub vortex due to the dominant behavior. As can be seen from Figure 11, the power density towards the 1700 Hz band is increasing, but higher frequency regions can not be observed because the resolved time step size limits the frequency range. When the sound directivity is examined, it is seen that the sound which propagates from the source and proceeds in wave form is strong in the blade region while the intensity decreases as it goes outward. It is clear that the sound directivity is frequency-dependent.

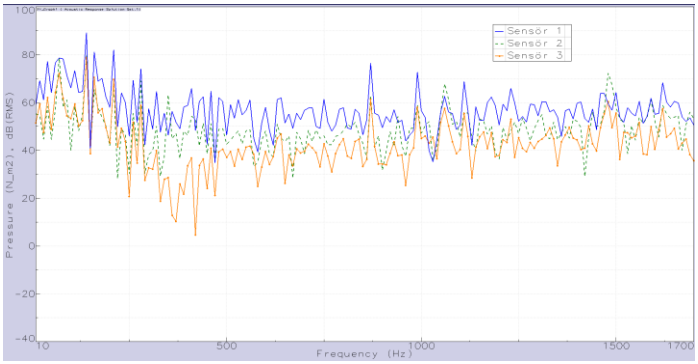

Figure 10. Numerical measurement of radiated noise from body at three different sensors

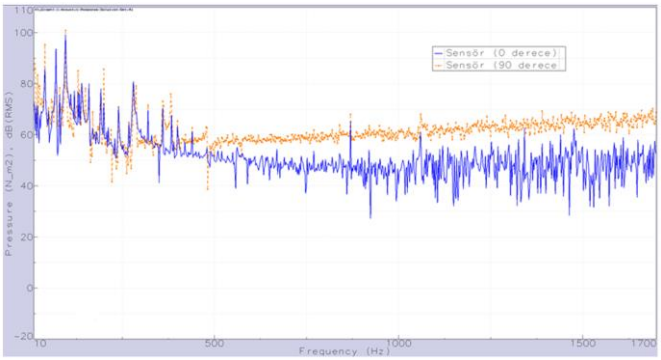

Figure 11. Numerical measurement of CRP radiated noise at three sensors

As can be seen from Figure 11, the power density towards the 1700 Hz band is increasing, but higher frequency regions can not be observed because the resolved time step size limits the frequency range. When the sound directivity is examined, it is seen that the sound which propagates from the source and proceeds in wave form is strong in the blade region while the intensity decreases as it goes outward. It is clear that the sound directivity is frequency-dependent.

5 CONCLUSION

In the article, hydroacoustic properties of a generic underwater vehicle are estimated by numerical methods. Hybrid approach between CFD and Lighthill analogy are used in an interdisciplinary case. Hydrodynamic scales are quite different from acoustic scales and direct solutions via DNS are unfortunately not possible in the

industrial field. For this reason, it is inevitable to resort to hybrid analogy solutions. The validity of the numerical method is investigated by performing various testcases aiming to see the accuracy of the numerical method. The validated method is applied to the acoustical simulation of underwater vehicle. The sources of dominant noise are questioned and the similar methodology can be used as guidance in design phase. Classification of acoustic traces in the spectrum has been given to point out different types of acoustical contributions. Sound pressure levels in simulation are determined by sound pressure receivers located at certain distances from the underwater vehicle. It has been demonstrated that the method can be applied to different platforms exposed to flow noise. Thus, acoustic trace classification, sound pressure level observation, sound propagation diagram can be obtained in acoustical solver by using time-dependant pressure data. It has been shown that the selection of the time dependent method and adequate number of cell in the volume is important. The acoustical finite mesh requires that the cell size must be at least one fifth of wave length in order to carry out mesh mapping at a sufficient level. Since acoustical operations are performed on LES basis, computations take time even if a high-speed and memory-intensive computer is used. Although the FEM solutions on the acoustic side are relatively short, the memory requirement is still high due to the intense matrix solutions. It seems possible to carry out further complementary work by including vibroacoustic elements in future studies. In this way, sound sources originating from vibration can be classified within the spectrum and studies for improving the structures can be realized.

REFERENCES

1. Brizzolara S., Villa D. and Gaggero S. (2011). SMP Workshop on Cavitation and Propeller Performances: The Experience of the University of Genova on the Potsdam Propeller Test Case, Second International Symposium on Marine Propulsors SMP11, Hamburg. German.

2. Güngör E. & Özdemir İ. B. (2015), Design and Analyses of a Propeller for Underwater Vehicles Using Computational Fluid Dynamics, Journal of Applied Mechanics and Materials, ISSN: 1662-7482, Vol. 798, pp 155-159.

3. Güngör E. (2015). Prediction of Performance of Test-Case Inclined Propeller SMP15 in Cavitating and Non Cavitating Conditions. Fourth International Symposium on Marine Propulsors smp'15. Austin, Texas, USA.

4. Sovani S. D. & Chen K. H. (2005). Aeroacoustics of an Automotive A-Pillar Raingutter: A Numerical Study with the Ffowcs-Williams Hawkings Method, SAE Noise and Vibration Conference and Exhibition. Traverse City, Michigan.

5. Rumpfkeil M. P., Robertson K. D., Visbal M. R. (2014). Comparison of aerodynamic noise propagation techniques. AIAA SciTech, 52nd Aerospace Sciences Meeting, Maryland.

6. Salvatore F., Testa C., and Greco L. (2009). Coupled Hydrodynamics-Hydroacoustics BEM Modelling of Marine Propellers Operating in a wakefield." First International Symposium on Marine Propulsors. Trondheim, Norway.

7. Oberai A., Ronaldkin F., Hughes T. (1963). Computational procedures for determining structural-acoustic response due to hydrodynamic sources, Comp. Methods Appl. Mech. Engineering 190, 345-361,2000.

8. Smagorinsky J. General circulation experiments with the primitive equations, Monthly Weather Review, Vol.93, No.3, pp99.

9. Curle N. (1955). The influence of solid boundaries upon aerodynamic sound. Proc. Royal Soc. 231A. Pp. 505-514, 1955.

10. Boswell J. R. (1971). "Design, cavitation performance, and open-water performance of a series of research skewed propellers," Department of the Navy Naval Ship Research Development Center, Washington, D.C.

11. Potsdam Experimental Team (2015). Proceedings of the Second Workshop on Cavitation and Propeller Performance, Fourth International Symposium on Marine Propulsors SMP15 . Austin, Texas, USA.